Dalton Transactions

ROYAL SOCIETY OF CHEMISTRY

COMMUNICATION

View Article Online
View Journal | View Issue

Check for updates

Cite this: *Dalton Trans.*, 2023, **52**, 2937

Received 23rd December 2022,
Accepted 22nd February 2023

DOI: 10.1039/d2dt04118a

rsc.li/dalton

Observation of two-step spin transition in iron(II) 4-amino-1,2,4-triazole based spin crossover nanoparticles†

Nikolia Lalioti, *[a] Efstathia Giannopoulou, [a] Alexander Charitos, [a] John Parthenios, [b] Ondrej Malina, *[c] Michaela Polaskova,[c] Alexandros Kalarakis [d] and Vassilis Tangoulis *[a]

A synthetically controllable two-step spin transition was observed in iron(II) spin crossover nanoparticles of the dehydrated one-dimensional coordination polymer $[Fe(NH_2trz)_3]Br_2$ (NH_2trz = 4-amino-1,2,4-triazole) using the reverse micellar method. The change from two-step to one-step hysteretic characteristics succeeded by changing the reaction time.

The temperature dependent spin state change of iron(II) from low-spin $S = 0$ to high-spin $S = 2$, known as spin crossover phenomenon (SCO), which is further accompanied by large thermal hysteretic phenomena at temperatures close to RT or above, has widened the horizons in the field of nano structuration of molecule-based devices.[1] It is therefore of utmost importance to correlate the SCO properties as a function of the size of SCO nanoparticles. Although there has been extensive research study for the case of 1D coordination polymers (CPs) of $[Fe(Htrz)(trz)_2]BF_4{\cdot}xH_2O$ [2–13] less attention is paid to the 1D CP of $[Fe(NH_2trz)_3](anion)_2{\cdot}xH_2O$. Conclusions have been drawn from studies in $[Fe(NH_2trz)_3]Br_2{\cdot}3H_2O$, according to which NPs with dimensions 30–50 nm present considerably reduced thermal hysteresis width to values close to 2 K and critical temperatures T_1 = 312 K, T_2 = 310 K.[14–16] For macroscopic or micrometric particles the upper limit of T_1 value was found to be 320 K with thermal width of 15 K.[14–16] For the above mentioned NPs (will be referenced as **NPL**) a reverse micellar method was followed using the non-ionic surfactant Lauropal playing the role of surfactant and oil. In 2002, Berezovskii *et al.*[17] described a dehydrated analogue of $[Fe(NH_2trz)_3]Br_2$ with higher critical temperatures 318 and 328 K suggesting different phases but unfortunately, no p-XRD diffractograms were presented. Recently, a two-step hysteretic behaviour has been observed[18] for the case of a single nanoparticle of $[Fe(NH_2trz)_3]Br_2$ by means of surface plasmon resonance microscopy (SRPM) and it was attributed to the existence of two physically contacted sub-regions behaving independently in the spin transition processes. Inspired by the previous studies we decided to pursue this research by introducing another untested surfactant into the above-mentioned system in order to enrich its poor nano-synthetic database as well as to investigate the effect of the surfactant to control crystal growth and size of the nano-products.

In the present work, we report the nano-synthesis and characterization of the 1-D SCO CP $[Fe(NH_2trz]_3Br_2$ using the reverse micellar synthetic method where we used the non-ionic TX100 as surfactant with *n*-hexanol as co-surfactant and cyclohexane as the organic solvent. The elemental analysis performed was consistent with the general formulas: $[Fe(NH_2trz)_3]Br_2{\cdot}3H_2O{\cdot}0.02TX100$ (**NP1**), $[Fe(NH_2trz)_3]Br_2{\cdot}3H_2O{\cdot}0.04TX100$ (**NP2**), $[Fe(NH_2trz)_3]Br_2{\cdot}3H_2O{\cdot}0.02TX100$ (**NP3**) indicating the presence of surfactant percentage (Table S1†).

The morphology and dimensions of the SCO NPs have been determined by Transmission Electron Microscopy (TEM) (Fig. S1 and Table S2†). For all cases, the particles are plate-like starting from well-defined elongated plates (**NP1**, mean size = 70 nm) to more irregular elongated plates (**NP2**, mean size = 70 nm) and discoidal-like (**NP3**, mean size = 60 nm). Similar sizes have been observed for **NPL** particles with 77% of Lauropal presenting completely spherical morphology while increasing the percentage of Lauropal to 85%, isolated spherical particles of 30 nm were obtained.[15] The structural characterization has been carried out by means of IR spectroscopy (Fig. S2 and Table S3†) and p-XRD (Fig. 1). Due to the poor crystallinity of the products no reliable indexing can be carried out. Nevertheless, **NP1–2** have similar diffractograms with very

[a]*Department of Chemistry, Laboratory of Inorganic Chemistry, University of Patras, 26504 Patras, Greece. E-mail: lali@upatras.gr, vtango@upatras.gr*
[b]*Institute of Chemical Engineering Sciences, Foundation of Research and Technology-Hellas (FORTH/ICE-HT), Stadiou Street, Platani, Patras, 26504 Greece*
[c]*Regional Centre of Advanced Technologies and Materials, Czech Advanced Technology and Research Institute (CATRIN), Palacký University Olomouc, Křížkovského 511/8, 77900, Czech Republic. E-mail: ondrej.malina@upol.cz*
[d]*Department of Mechanical Engineering, University of the Peloponnese, 26334 Patras, Greece*

†Electronic supplementary information (ESI) available: Experimental details, IR spectra, TEM images, DSC measurements, Raman spectra and tables. See DOI: https://doi.org/10.1039/d2dt04118a

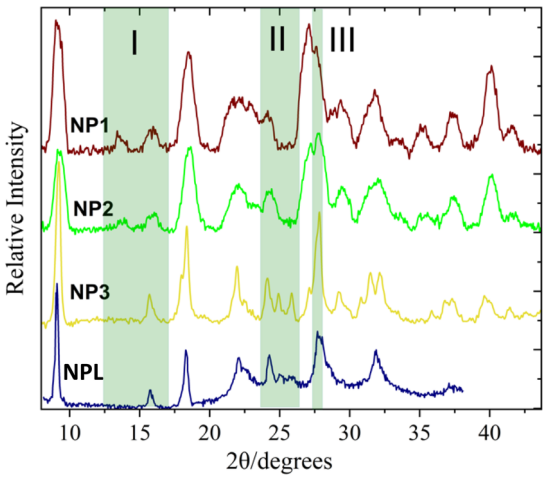

Fig. 1 p-XRD diffractograms of the SCO **NP1–3**. The highlighted regions are focused on the differences between the patterns of the NPs **1–2** and NPs **3**. **NPL** represents the diffractogram from ref. 15.

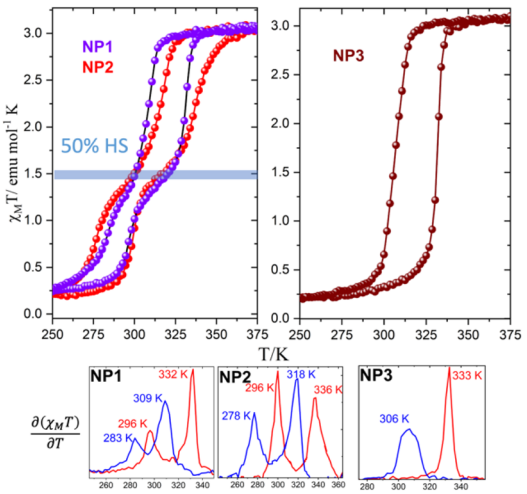

Fig. 2 Temperature dependence of the susceptibility data of the dehydrated SCO **NP1–3** (third cycle) for the sweep rate of 1 K min^{-1}. The onset of the second step is defined with the percentage of the HS fraction as a solid bar. The first derivatives of the thermal hysteresis are shown as red lines for the heating mode and blue lines for the cooling mode.

close intensities while **NP3**, interestingly, share similar characteristics with the **NPL** particles (especially the case of 85% of Lauropal)[15] and distinctive differences from **NP1–2** in three different 2θ regions (depicted as I, II, II in Fig. 1). Calculation of the crystallite sizes has been carried out using the Scherrer equation and the apparent size of the crystallites, $\langle L_V \rangle$, was derived in Table S2† along with the diameter of the average domain, $\langle D \rangle$, assuming spherical domains. Also, taking into account that the volume occupied by an entity of $[Fe(NH_2trz)_3]Br_2{\cdot}3H_2O$ in the crystal solid[19] is close to 40 Å^3 it was possible to calculate the average number of domains per particle, $\langle N_D \rangle$. According to the findings, the particle size seems to be inversely proportional to the diameter of the coherent domain in agreement with the literature.[15]

Thermogravimetric measurements performed for **NP1–3** in the temperature loop 20–130–20 °C revealed the same overall behaviour (Fig. S3†). An abrupt loss of 2–5% weight is noticed at room temperature and complete dehydration which corresponds to the removal of approximately three lattice water molecules, (loss of almost 10% weight) is succeeded during the heating mode at temperatures close to 120 °C.[15] DLS measurements for the ethanolic dispersion of NPs (Fig. S4†) revealed mean sizes of 155 nm, 155 nm, and 120 nm for **NP1–3** respectively. The estimated PDI values are close to 0.23 for all cases suggesting good quality of the colloid in ethanol.

To avoid any influence of the lattice water molecules within the iron chains a modified experimental protocol was followed for the magnetic measurements according to which: (a) the sample is pre-heated to 400 K for 2 h and (b) three thermal cycles were performed in the temperature sequence (400 K–200 K–400 K) with a rate of 1 K min^{-1}. The third thermal cycle of the **NP1–3** in the temperature range 200–400 K is presented in Fig. 2. Quite unexpectedly, **NP1–2** reveal for the first time, a two-step hysteretic behaviour where the first high temperature step (HT step) is well above the usual critical temperatures expected for the $[Fe(NH_2trz)_3]Br_2{\cdot}xH_2O$.[14–16] More explicitly, the critical temperatures of the high temperature (HT) step derived from the temperature dependence of the first derivative are: $T_{1/2}\uparrow$ = 332 K/336 K and $T_{1/2}\downarrow$ = 309 K/318 K with hysteresis widths of 22 K/18 K while for the second low temperature (LT) step are: $T_{1/2}\uparrow$ = 296 K/296 K and $T_{1/2}\downarrow$ = 283 K/278 K with hysteresis widths of 13 K/18 K for **NP1–2** respectively. The SCO **NP3** reveal a one-step hysteretic behaviour with $T_{1/2}\uparrow$ = 333 K and $T_{1/2}\downarrow$ = 306 K and width of 27 K. For all the SCO **NP1–3** the $\chi_M T$ at room temperature is 3.1 emu mol^{-1} K close to the value expected for an iron(II) compound in the HS state while at temperatures lower than 250 K, where the LS state is populated, the $\chi_M T$ is close to 0.25 emu mol^{-1} K suggesting that 10% of the NPs remains in its HS state. The high spin fraction observed after cooling is attributed to the weakening of iron(II) ligand field due to the replacement of nitrogen atoms by water ligands.[14–16] Interestingly, the onset of the second step is close to 50% of the HS fraction for the case of SCO **NP1–2** and disappeared for the case of SCO **NP3**.

Fast sweep-rate dependent magnetic measurements at 5 and 10 K min^{-1} have been performed to further investigate the two step behavior and the results are shown in Fig. 3, Fig. S5 and Table S4.† For the case of **NP1–2**, the two steps are smeared out at 10 K min^{-1} with critical temperatures $T_{1/2}\uparrow$ = 326 K/328 K; $T_{1/2}\downarrow$ = 292 K/292 K and width of 34 K/36 K respectively. The SCO **NP3** retains its one step behaviour in all three different sweep rates and although the critical temperature of the heating branch remains almost the same at *ca.* 335 K the $T_{1/2}\downarrow$ is shifted to 290 K at 10 K min^{-1} revealing the largest width, 45 K, ever observed for this family of SCO NPs. For the case of **NP3** long metastable state lifetimes are involved[20,21] while for **NP1–2** the disappearance of the steps at

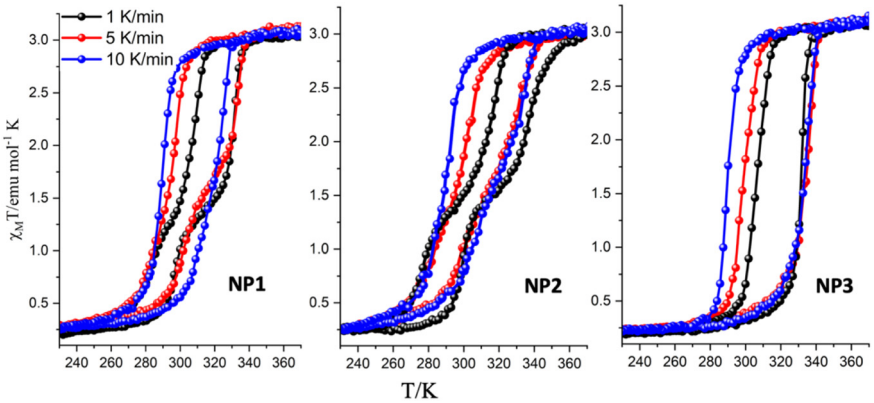

Fig. 3 Temperature dependence of the susceptibility data of the dehydrated SCO **NP1–3** (third cycle) for sweep rates of 1 K min^{-1}, 5 K min^{-1} and 10 K min^{-1}.

high sweep rates implies the occurrence of a phase transition that takes place more slowly than the spin transition.

Generally, the appearance of a two-step ST in the case of 1D iron(II) chains is related to: (a) antagonistic intrachain interactions between equivalent or non-equivalent iron(II) centres due to zigzag chain structure; (b) the presence of non-equivalent iron(II) centres in the chain; and (c) chain length distribution of short and long chains.[22,23] The first case is excluded for the understudy 1D polymer based on the crystal structure of the 1D CP $[Fe(NH_2trz)_3](NO_3)\cdot xH_2O$ [19] while both the other cases are possible reasons for the two-step ST behaviour. According to the above-mentioned crystal structure analysis the solid is crystallized in the triclinic space group $P\bar{1}$ with two non-equivalent iron atoms to be located on adjacent centres of inversion along the *a* direction. Furthermore, the possibility of different polymorphs, cannot be excluded.

The reaction system was studied in two different ω_o (4, 10) *i.e.* different proportions of the oily phase components and also different completion times of the micellar exchange. The procedure was repeated several times to confirm the reproducibility of NPs synthesis. NPs characterization suggested that changing the ω_o from 4 to 10 mainly affects the percentage of TX100 that remains attached to the NPs *i.e.* **NP1** and **NP3** have a smaller percentage of TX100 than **NP2** where the organic phase mixture contained a larger amount of TX100. The reaction time seems to be decisive both in the high yield of the product and in better morphological uniformity as seen in **NP3** where the reaction time was twice as long (2 days). The high solubility of $FeBr_2\cdot 6H_2O$ and NH_2trz in water makes it difficult to prepare saturated aqueous phases.

From the magnetic point of view the two-step hysteretic phenomena are observed at low magnetic sweep-rates and only for the case of **NP1–2**. A drastic change in the magnetic characteristics of the thermal hysteresis occurred for the case of **NP3** (ω = 10 and reaction time = 2 days) where a single step thermal hysteresis is observed at all sweep rates.

The SCO phenomenon of **NP1–3** was further investigated by differential scanning calorimetry over the temperature range 250–400 K at 10 K min^{-1} and the results of the 3rd cycle are shown in Fig. S6† in agreement with the magnetic results (Table S4†). To avoid the lattice water molecules that remain trapped during the warming-cooling cycles we performed the DSC measurements in a pin-hole hermetic aluminum pan under an inert gas flow.[24,25]

A Raman laser power-assisted protocol was used to investigate the SCO phenomenon of the **NP1–3** according to which the LS state was monitored for all the NPs through exposure of 150 s at laser power equal to 84 μW while the HS state was activated by increasing the laser power to 340 μW at the same exposure time. Raman spectra of **NP1–3** in the LS and HS states are shown in Fig. 4 and S7† while the peak assignment of the LS spectra is presented in Table S5.† According to the assignment the bending mode of the amino group is located at 1616 cm^{-1} while the coupled stretching modes of C–C and N–N of the triazole ring are presented in the range 600–1545 cm^{-1}.[26] Bending and torsion vibrations of intra-

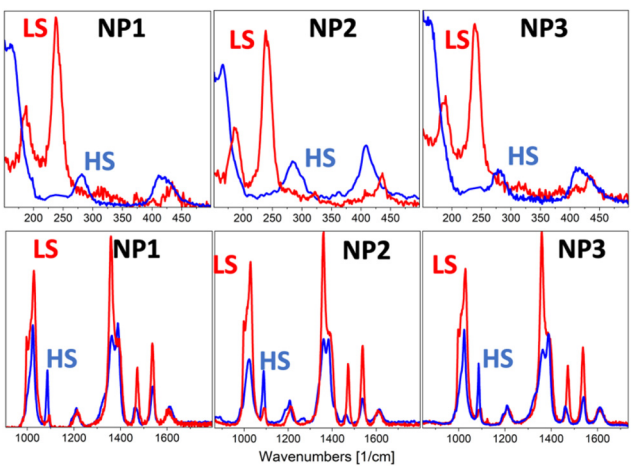

Fig. 4 Comparison of HS Raman spectra (blue line) and LS Raman spectra (red line) of **NP1–3** in the range of 150–500 cm^{-1} and 850–1700 cm^{-1}.

molecular nature depending strongly on the strength of the Fe–N interaction give rise to a small number of low-intensity bands in the range of 150–500 cm^{-1}. The peaks in the range 150–300 cm^{-1} of the LS Raman spectra are used as a "fingerprint" of the spin transition since these peaks disappear in the HS state[14] in accordance with the experimental results presented in Fig. 4 for the **NP1–3**.

In conclusion, we presented a synthetically controllable two-step spin transition in iron(II) SCO NPs of the dehydrated type of 1D CP $[Fe(NH_2trz)_3]Br_2$ using a reverse micellar method with a non-ionic surfactant TX100. According to our study changing the ω_o from 4 to 10 mainly affects the percentage of TX100 that remains attached to plate-like NPs of 60–70 nm. The two-step hysteretic phenomena are observed at low magnetic sweep-rates of 1 K min^{-1} and for reaction time of 20 h (**NP1–2**). A drastic change in the magnetic characteristics of the thermal hysteresis occurred for the case of **NP3** (ω = 10 and reaction time = 2 days) where a single step thermal hysteresis is observed at all sweep rates. In all cases the critical temperatures observed are well above the usual values expected for the $[Fe(NH_2trz)_3]Br_2{\cdot}xH_2O$. For the case of **NP1–2**, the two-steps are smeared out at 10 K min^{-1} while **NP3** retains its one step behaviour in all three different sweep rates and although the critical temperature of the heating branch remains almost the same at *ca.* 335 K the $T_{1/2}\downarrow$ is shifted to 290 K at 10 K min^{-1} revealing the largest width, 45 K, ever observed for this family of NPs. A Raman laser power-assisted protocol was used to monitor the SCO phenomenon of the NPs. Further study is underway on both the (ω, t) synthetic factors as well as FORC, modulate DSC and Mössbauer measurements.

Conflicts of interest

There are no conflicts to declare.

Acknowledgements

O. M. and M. P. would like to thank to the following projects: the Research Infrastructure NanoEnviCz, supported by the Ministry of Education, Youth and Sports of the Czech Republic under Project No. LM2018124 and the ERDF/ESF project "Nano4Future" (No. CZ.02.1.01/0.0/0.0/16_019/0000754) of the Ministry of Education, Youth and Sports of the Czech Republic.

References

1 R. Sanchez-de-Armas, N. Montenegro-Pohlhammer, A. Develioglu, E. Burzuri and C. J. Calzado, *Nanoscale*, 2021, **13**, 18702–18713.
2 M. Gimenez-Marques, M. L. Garcia-Sanz de Larrea and E. Coronado, *J. Mater. Chem. C*, 2015, **3**, 7946–7953.
3 E. Coronado, J. R. Galán-Mascarós, M. Monrabal-Capilla, J. García-Martínez and P. Pardo-Ibáñez, *Adv. Mater.*, 2007, **19**, 1359.
4 J. R. Galán-Mascarós, E. Coronado, A. Forment-Aliaga, M. Monrabal-Capilla, E. Pinilla-Cienfuegos and M. Ceolin, *Inorg. Chem.*, 2010, **49**, 5706.
5 S. Titos-Padilla, J. M. Herrera, X.-W. Chen, J. J. Delgado and E. Colacio, *Angew. Chem., Int. Ed.*, 2011, **50**, 3290.
6 A. A. Blanco, D. J. Adams, J. D. Azoulay, L. Spinu and J. B. Wiley, *Molecules*, 2022, **27**, 1213.
7 J. M. Herrera, S. Titos-Padilla, S. J. a. Pope, I. Berlanga, F. Zamora, J. J. Delgado, K. V. Kamenev, X. Wang, A. Prescimone, E. K. Brechin and E. Colacio, *J. Mater. Chem. C*, 2015, **3**, 7819.
8 I. Suleimanov, J. S. Costa, G. Molnár, L. Salmon and A. Bousseksou, *Chem. Commun.*, 2014, **50**, 13015.
9 S. Rat, M. Piedrahita-Bello, L. Salmon, G. Molnár, P. Demont and A. Bousseksou, *Adv. Mater.*, 2018, **8**, 1705275.
10 M. Piedrahita-Bello, K. Ridier, M. Mikolasek, G. Molnár, W. Nicolazzi, L. Salmon and A. Bousseksou, *Chem. Commun.*, 2019, **55**, 4769.
11 R. Torres-Cavanillas, L. Lima-Moya, F. D. Tichelaar, H. W. Zandber-gen, M. Giménez-Marqués and E. Coronado, *Dalton Trans.*, 2019, **48**, 15465.
12 P. Gkolfi, D. Tsivaka, I. Tsougos, K. Vassiou, O. Malina, M. Polaskova, C. D. Polyzou, C. T. Chasapis and V. Tangoulis, *Dalton Trans.*, 2021, **50**, 13227.
13 C. D. Polyzou, P. Gkolfi, C. T. Chasapis, V. Bekiari, A. Zianna, G. Psomas, O. Malina and V. Tangoulis, *Dalton Trans.*, 2022, **51**, 12427.
14 T. Forestier, S. Mornet, N. Daro, T. Nishihara, S. Mouri, K. Tanaka, O. Fouche, E. Freysz and J. F. Letard, *Chem. Commun.*, 2008, 4327–4329.
15 T. Forestier, A. Kaiba, S. Pechev, D. Denux, P. Guionneau, C. Etrillard, N. Daro, E. Freysz and J. F. Letard, *Chem. – Eur. J.*, 2009, **15**, 6122–6130.
16 A. Rotaru, F. Varret, A. Gindulescu, J. Linares, A. Stancu, J. F. Letard, T. Forestier and C. Etrillard, *Eur. Phys. J. B*, 2011, **84**, 439–449.
17 G. A. Berezovskii and V. G. Bessergenev, *Russ. J. Phys. Chem.*, 2002, **76**, 1246.
18 S. S. Liu, K. Zhou, T. L. Yuan, W. R. Lei, H. Y. Chen, X. Y. Wang and W. Wang, *J. Am. Chem. Soc.*, 2020, **142**, 15852–15859.
19 A. Grosjean, N. Daro, B. Kauffmann, A. Kaiba, J. F. Letard and P. Guionneau, *Chem. Commun.*, 2011, **47**, 12382–12384.
20 S. Brooker, *Chem. Soc. Rev.*, 2015, **44**, 2880–2892.
21 R. Kulmaczewski, J. Olguin, J. A. Kitchen, H. L. C. Feltham, G. N. L. Jameson, J. L. Tallon and S. Brooker, *J. Am. Chem. Soc.*, 2014, **136**, 878–881.
22 S. M. Neville, B. A. Leita, G. J. Halder, C. J. Kepert, B. Moubaraki, J. F. Letard and K. S. Murray, *Chem. – Eur. J.*, 2008, **14**, 10123–10133.

23 M. M. Dirtu, F. Schmit, A. D. Naik, I. Rusu, A. Rotaru, S. Rackwitz, J. A. Wolny, V. Schunemann, L. Spinu and Y. Garcia, *Chemistry*, 2015, **21**, 5843–5855.
24 M. B. Bushuev, D. P. Pishchur, I. V. Korolkov and K. A. Vinogradova, *Phys. Chem. Chem. Phys.*, 2017, **19**, 4056–4068.
25 O. Roubeau, M. Castro, R. Burriel, J. G. Haasnoot and J. Reedijk, *J. Phys. Chem. B*, 2011, **115**, 3003–3012.
26 Y. A. Tobon, L. Kabalan, S. Bonhommeau, N. Daro, A. Grosjean, P. Guionneau, S. Matar, J. F. Letard and F. Guillaume, *Phys. Chem. Chem. Phys.*, 2013, **15**, 18128–18137.